WARSAW UNIVERSITY OF TECHNOLOGY Index 351733
FACULTY OF CIVIL ENGINEERING
COMMITTEE FOR CIVIL AND WATER ENGINEERING
POLISH ACADEMY OF SCIENCES ISSN 1230-2945

DOI: 10.24425/ace.2024.149887

ARCHIVES OF CIVIL ENGINEERING

Vol. LXX ISSUE 2 2024

pp. 661 –675

Research paper

Hydration heat generation and dissipation in diaphragm walls

Łukasz Grabowski[1], Monika Mitew-Czajewska[2]

Abstract: This study focuses on the complex dynamics of heat dissipation within diaphragm walls during concrete hydration, crucial in construction engineering. Experimental measurements from three sites in Poland, featuring diaphragm walls of varying thicknesses, ranging from 1 to 1.5 meters, were compared to a numerical model. The model, using a Finite Difference Method, incorporated stages of execution of adjacent panels and their thermal influence. The results closely mirrored the measured temperatures, validating the accuracy of its predictions. Despite minor discrepancies, mostly within ±3°C, the method effectively approximated real-life scenarios. Suggestions for model enhancements include incorporating the effect of concrete admixtures and refining the modeling of sequential panel execution. The thermal soil parameters, their possible range, and their impact on hydration heat dissipation in deep foundations emerged as crucial insights. This research serves as a foundation for deeper investigations into early-age behavior in deep foundations, aiming to extend the analysis to stress and strain domains to unravel characteristic cracking patterns observed in diaphragm walls.

Keywords: deep foundations, diaphragm walls, hydration heat, early age thermal cracking, tremie concrete

[1]MSc Eng., Warsaw University of Technology, Faculty of Civil Engineering, Al. Armii Ludowej 16, 00-637 Warsaw, Poland, Soletanche Polska Sp. z o.o., Al. "Solidarności" 173 bud. C, 00-877 Warsaw, Poland, e-mail: lukasz.grabowski6@pw.edu.pl, ORCID: 0000-0002-1599-2407

[2]DSc., PhD., Eng., Warsaw University of Technology, Faculty of Civil Engineering, Al. Armii Ludowej 16, 00-637 Warsaw, Poland, e-mail: mm@il.pw.edu.pl, ORCID: 0000-0002-2651-2026

1. Introduction

In the realm of construction and civil engineering, the phenomenon of heat dissipation within concrete elements due to the exothermic reactions of cement hydration stands as a crucial area of study. The heat generated during this hydration process usually impacts the freshly cast elements, rarely significantly affecting the surrounding environment or objects in the vicinity. Such is the case with concrete structures built overground. Due to a large contact surface with the atmosphere, most heat is dissipated through convection and radiation, while a relatively small contact surface with the rest of the structure limits conductive heat transfer.

For foundations, especially the deep ones, the exact opposite is true. Convective heat transfer can be neglected except for very specific cases of intensive filtration. Heat is dissipated through conduction to the soil around it. This apparent simplification of the phenomenon in terms of physics is balanced by the complexity of the real-life processes of the construction site. Constructing deep foundations is usually highly dependent on the technology of execution. It often comprises several stages of works, in which the time component is not negligible. From the physics perspective, this creates a transient set of conditions that influence the heat flow. Complex thermal behavior in the early stages of the concrete life cycle also influences the stress state.

Young concrete is subject to thermal gradients due to hydration heat discharge, and autogenic and drying shrinkage. Together, these phenomena create a strain field that must be resisted by young concrete; otherwise, the cracking will occur. The causes of cracking are considered in two approaches. If we take the temperature and shrinkage effects within an arbitrary cross-section of a concrete element during curing (Fig. 1), we observe differences in strains across the thickness of the element.

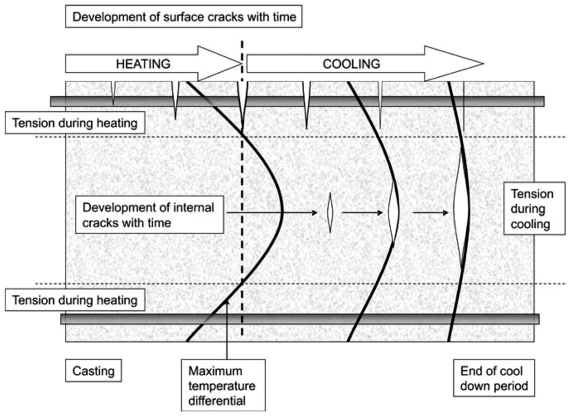

Fig. 1. Thermal cracking development with time [1]

The shrinkage is considered to be driven by the degree of hydration [2], although it has been demonstrated that it is also dependent on the water-cement ratio [3]. While the degree of hydration is not uniform across the element, the shrinkage differences are considered

negligible in practice [1]. On the other hand, the temperature gradient can be considerable and is the main effect causing differential strains. Those differential strains are resisted by the concrete, resulting in self-induced stresses in a situation called "internal restraint".

The freedom of the concrete element to expand can additionally be limited by external means, like connections with previously cast structures or friction. The temperature and shrinkage again play a major role as the main factors influencing strains. This time the entire concrete element is considered with external boundary conditions and mean internal temperature and shrinkage strains. Again, any expansion or contraction resisted by external forces creates additional restraint stresses in a situation called "external restraint".

Both internal and external restraint happen simultaneously while strength and elastic modulus increase due to curing. It is known that allowing excessive restrained strains to arise in concrete elements at an early age can lead to different types of cracking [4]. In typical cases, there are available measures that can be taken to limit the risk of cracking [5].

For deep foundations, the array of possibilities is severely limited due to technological constraints. On the other hand, the consequences could be affecting a wide range of aspects of a construction site. Starting from serviceability, the cracks can be detrimental in all three aspects of crack control indicated by Eurocode 2 [6] – appearance, durability, and proper functioning. Excessive crack width is detrimental to durability and appearance, while proper functioning can be influenced by the inflow of groundwater through cracks if not sealed. Sealing of cracks is costly, usually needs to be done iteratively, and may also negatively influence the works schedule.

The only case of a peer-reviewed article on the cracking of a deep foundation – a diaphragm wall – was described in the '90 s in [7, 8]. The author pointed to the thermal gradient as the main cause of cracking. A characteristic pattern was noted where secondary panels were cracked more significantly. The pattern of cracks is shown in Fig. 2.

Fig. 2. Cracking of diaphragm wall on Kawasaki Island [7]

The above demonstrates that understanding and anticipating these thermal effects is paramount not only for ensuring the serviceability of the structures but also for minimizing potential contractual implications. Still, there is little research done on real-life foundation structures. There are, however, similar attempts [9] to predict real-life conditions based on temperature measurements and numerical modelling. This article concentrates on predicting the development of temperatures within deep foundations through numerical modeling and comparison with experimental data.

2. Experimental measurements of diaphragm walls temperatures

2.1. General information

Experimental data were collected on 3 separate construction sites in Poland. All of these large infrastructural works were selected because the thickness of their designed diaphragm walls was at least 1 m. The choice of the minimum thickness was based on own numerical analysis as well as on indications in literature [1, 7, 10] as to the predicted magnitude of temperature gradients.

2.2. Measurement methodology

In order to measure temperature and strains during early age, the embedment vibrating-wire strain gauges were used. These gauges work by measuring the frequency of an agitated wire [11]. The relation between the frequency and stress in the wire is given by Eq. (2.1).

$$f = \frac{1}{2L} \cdot \sqrt{\frac{\sigma}{\rho}} \tag{2.1}$$

where: L – length of vibrating wire (m), σ – wire stress (N/m^2), ρ – density (kg/m^3), f – natural frequency (Hz).

The corresponding strain can be calculated from the wire stress by using Hooke's Law and by applying correction on different thermal expansion coefficients of steel and concrete.

Vibrating wire gauges come equipped with NTC thermistors that are located in mid-span, close to the coil. Thermistors are resistors made of materials that display a large difference in resistance in function of temperature [11]. The relation between resistance and temperature is given by the Steinhart-Hart equation (Eq. (2.2)) below:

$$\frac{1}{T} = A + B \ln R + C (\ln R)^3 \tag{2.2}$$

where: T – temperature (K), R – resistance (Ω), A, B, C – thermistor coefficients, provided by the manufacturer, $\ln X$ – natural logarithm of X, logarithm in base e.

2.3. Gauges installation

The gauges were installed in reinforcement cages of the diaphragm walls prior to the installation of the cage in the trench.

For the first test site (POK), a total of 2 installation locations were chosen to capture the temperature development in the core of the d-wall panel and at the edges of the panel. For each measurement point, there were 3 strain gauges – 2 at the opposite edges of the panel and one in the middle (Fig. 3).

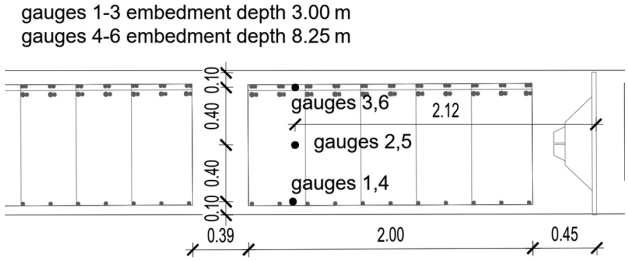

Fig. 3. Gauges locations on POK test site

For the second test site (LWK), a total of 4 installation locations in 2 panels were chosen: for the primary panel, 2 locations in the middle and 1 close to the edge of the panel; for the secondary panel, 1 location close to the edge of the panel (Fig. 4).

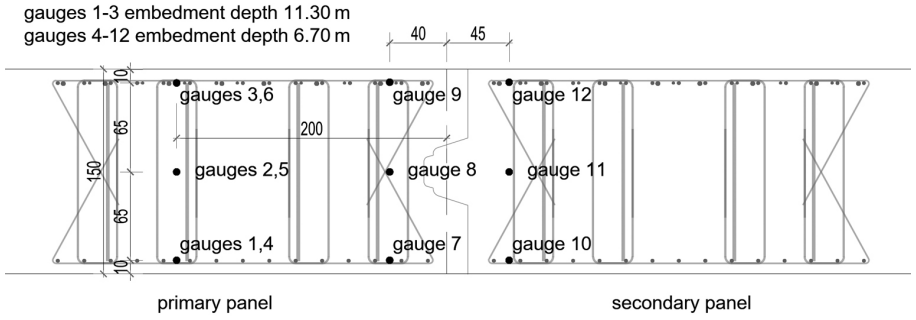

Fig. 4. Gauges locations on LWK test site

For the third test site (WZA), a total of 4 installation locations were chosen in 2 panels – 1 location in the middle and 1 close to the edge for each of the panels (Fig. 5).

The gauges were preinstalled in the locations shown above, several hours before installation of the cage into the trench. This process was crucial for the success of the measurement on each test site, as this is when the gauges are most likely to be damaged. When the reinforcement cage was placed, the cables were connected to the datalogger device, and the measurements were initiated with a frequency of 1 per hour. The measurement data were collected in a logging device and stored on an internal drive or sent to a remote server. Tabl 1 below shows the starting and ending dates of each measurement campaign.

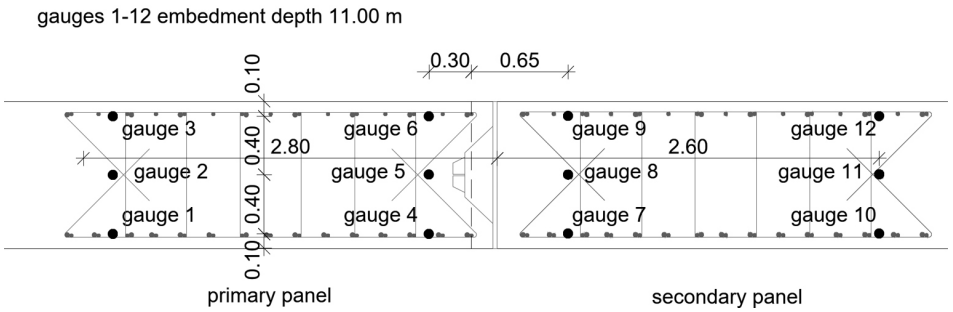

Fig. 5. Gauges locations on WZA test site

Table 1. Dates of measurements campaigns

Site	Starting date	Ending date
POK	07/07/2021	19/08/2021
LWK	14/12/2021	05/01/2022
WZA	30/01/2023	14/02/2023

3. Numerical analysis

3.1. Theoretical basis of calculations

The heat diffusion in an opaque solid body is described in general form by the differential equation (3.1):

$$c_p \rho \frac{\partial u}{\partial t} = \nabla (\lambda \nabla T) + \dot{Q}''' \tag{3.1}$$

where: T – temperature, t – time, $\dot{Q}'''$ – heat generation rate per unit volume, ρ – density, λ – thermal conductivity, c_p – specific heat.

Both the heat conduction coefficient and specific heat of the concrete vary during the cement hydration process [1, 12].

The heat generation rate term depends on the hydration reaction kinetic. Several researchers [13–15] have proven that the Arrhenius equation (Eq. (3.2) accurately describes the cement hydration reaction as a function of temperature.

$$k = A \cdot e^{\frac{-E_a}{RT}} \tag{3.2}$$

where: k – reaction rate constant, T – temperature (K), E_a– activation energy (J/mol), R – universal gas constant 8.3144 J/(mol·K), A – proportionality factor.

Based on Eq. (3.2) an equivalent age function Eq. (3.3) has been developed [14] to take into account the effect of varying temperature history on the hydration rate. The degree of

hydration can now be expressed as a function of the equivalent age in Eq. (3.4) as proposed in [16]. Then hydration heat over time can be expressed by Eq. (3.5) [17].

$$t_e\,(T_{\text{ref}} = 20^{\circ}\text{C}) = \int_0^t e^{\left(-\frac{E_a}{\text{R}}\left(\frac{1}{273+T}-\frac{1}{273+20}\right)\right)}\text{d}t \tag{3.3}$$

$$\alpha\,(t) = \alpha_u \cdot e^{-\left(\frac{\tau}{t_e}\right)^{\beta}} \tag{3.4}$$

$$\alpha\,(t) = \frac{Q\,(t)}{Q_{\text{tot}}} \tag{3.5}$$

To complete the above equations, researchers in [13, 18–20] studied the influence of cementitious material composition in concrete mix and presented the following Eqs. (3.6)–(3.11):

$$\alpha_u = \frac{1.031 \cdot \text{w/c}}{0.194 + \text{w/c}} + 0.50p_{\text{pfa}} + 0.30p_{\text{ggbs}} \tag{3.6}$$

$$E_a = 22100 \cdot \left(1 - 1.05 \cdot p_{\text{pfa}} \cdot \left(1 - \frac{p_{\text{fa-CaO}}}{0,40}\right) + 0.40 \cdot p_{\text{ggbs}}\right) \cdot p_{\text{C}_3\text{A}}^{0.30} \cdot p_{\text{C}_4\text{AF}}^{0.25} \cdot \text{Blaine}^{0.35} \tag{3.7}$$

$$\tau = 66.78 \cdot p_{\text{C}_3\text{A}}^{-0.154} \cdot p_{\text{C}_3\text{S}}^{-0.401} \cdot \text{Blaine}^{-0.804} \cdot p_{\text{SO}_3}^{-0.758} \cdot e^{2.187 \cdot p_{\text{ggbs}}} + 9.50 \cdot p_{\text{pfa}} \cdot p_{\text{pfa-CaO}} \tag{3.8}$$

$$\beta = 181.4 \cdot p_{\text{C}_3\text{A}}^{0.146} \cdot p_{\text{C}_3\text{S}}^{0.227} \cdot \text{Blaine}^{-0.535} \cdot p_{\text{SO}_3}^{0.558} \cdot e^{-0.647 \cdot p_{\text{ggbs}}} \tag{3.9}$$

$$Q_{\text{tot,cem}} = 500p_{\text{C}_3\text{S}} + 260p_{\text{C}_2\text{S}} + 866p_{\text{C}_3\text{A}} + 420p_{\text{C}_4\text{AF}} + 624p_{\text{SO}_3} + 1186p_{\text{CaO}} + 850p_{\text{MgO}} \tag{3.10}$$

$$Q_{\text{tot}} = Q_{\text{cem,tot}} \cdot p_{\text{cem}} + 461p_{\text{ggbs}} + 1800 \cdot p_{\text{fa}} \cdot p_{\text{fa-CaO}} + 330p_{\text{sf}} \tag{3.11}$$

where: Q_{tot} – total heat of hydration per unit of cement weight, w/c – water – cement ratio, Blaine – specific surface (m^2/kg) measured using Blaine method, p_{xxx} – mass fraction of component *xxx*, with pfa – pulverized fly ash, ggbs – ground granulated blast-furnace slag, sf – silica fume, C_3S – tricalcium silicate, C_2S – dicalcium silicate, C_3A – tricalcium aluminate, C_4AF – tetracalcium aluminoferrite, SO_3 – sulfur trioxide, CaO – calcium oxide, fa-CaO – calcium oxide in fly ash, MgO – magnesium oxide.

Collecting all of the above equations into the expression for $Q(t)$ and calculating the derivative with respect to time finally gives Eq. (3.12).

$$\dot{Q}''' = C \cdot Q_{\text{tot}} \cdot \alpha_u \cdot e^{-\left(\frac{\tau}{t_e}\right)^{\beta}} \cdot \left(\frac{\tau}{t_e}\right)^{\beta} \cdot \frac{\beta}{t_e} \cdot e^{-\frac{E_a}{R}\left(\frac{1}{273+T}-\frac{1}{293}\right)} \tag{3.12}$$

where: C – cementitious materials content (kg/m^3).

3.2. Numerical model

For solving the posed problem of heat diffusion with heat generation a Finite Difference Method (FDM) was employed. The governing Eq. (3.1) in 2D form was discretized using the Euler backward method [21] i.e. forward difference in time and central difference in space (FTCS). This approach is numerically the simplest approach, in which temperature at each point in time can be calculated from temperature values in the previous step. A disadvantage of using this method is the stability criteria that must be met to obtain a meaningful result. The stability of the solution was ensured by satisfying condition Eq. (3.13) [22] linking time and space steps:

$$\Delta t \leq \frac{\Delta x^2}{2\alpha\,(2 + h\Delta x)} \tag{3.13}$$

where: Δx – space step (m), Δt – time step (s), α – thermal diffusivity (m^2/s), h – heat tranfer coefficient ($W/(m^2 \cdot K)$).

Boundary conditions of the model are taken in the form of a convective boundary condition assuming heat flux dependent on the temperature difference between the edge and hypothetical temperature of the outer medium at a great distance from the model boundary. It takes the general form of Eq. (3.14):

$$q = h\left(T_{\text{edge}} - T_{\infty}\right) \tag{3.14}$$

where: q – heat flux (W/m^2), T_{edge} – temperature at model edge (K), T_{∞} – temperature of outer medium (K).

Boundary conditions assume no heat flux ($h = 0$) through boundaries that lie on the planes of symmetry. Since the heat transfer coefficient h at the boundary is generally unknown, the size of the model was chosen so that the value of h does not significantly influence the result within the time scope of the analysis. In such a case, $h = 0$ can be adopted for all boundaries.

The model adopted in the calculations takes advantage of the symmetry and contains ¼of the panel and soil around it (Fig. 6). The size of the model is arbitrarily taken as $L_x = B = 6$ m, which corresponds to the typical panel length and $L_y = 3H$, where H is nominal panel thickness.

Initial conditions include starting temperatures of concrete and soil. It is assumed that for $t = 0$ concrete temperature T_{conc} is taken from measurements and soil temperature is $T_{\text{soil}} = T_{\infty}$. For test sites, LWK and WZA construction stages of the adjacent panel are included in the analysis.

Construction stages in the model are represented by 3 calculation phases:

1. Primary panel concreting,
2. Slurry trench excavation of secondary panel (constant temperature of bentonite assumed),
3. Secondary panel concreting, each with rapid changes of temperature and material parameters between them.

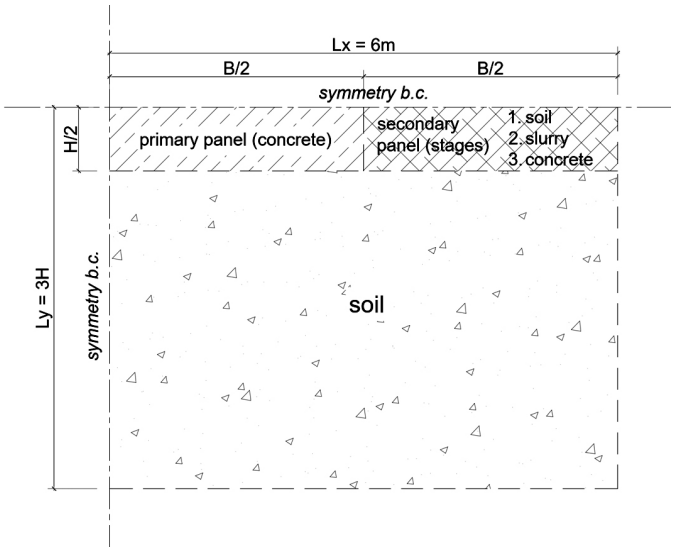

Fig. 6. Model scheme

Model parameters are presented in Table 2, concrete mixes for each test site are presented in Table 3, concrete parameters in Table 4, and concrete and hydration parameters in the model are presented in Table 5.

Table 2. Model dimensions and soil parameters

Site	Grid step dx	$L_x = B$	$L_y = 3H$	soil temp $T_{soil} = T_\infty$	soil vol. density ρ_{soil}	soil thermal conductivity λ_{soil}	soil specific heat $c_{p,soil}$
	m	m	m	°C	kg/m^3	W/(m·K)	kJ/(kg·K)
POK	0.05	6.0	3	9.5	2100	1.80	1.30
LWK			4.5				
WZA			3				

Table 3. Concrete mixes

Site	Cement type	Cement content	Fly ash content	Aggregates	w/cm
		kg/m^3	kg/m^3	kg/m^3	–
POK	CEM III/A	400	0	1655	0.41
LWK	CEM III/A	300	100	1730	0.41
WZA	CEM III/A	320	80	1720	0.41

Table 4. Concrete parameters

Site	Cast temp primary $T_{\text{conc,prim}}$	Slurry temp T_{slurry}	Cast temp secondary $T_{\text{conc,second}}$	Vol. density ρ_{conc}	Thermal conductivity λ_{conc}	Specific heat $c_{p,\text{conc}}$
	°C	°C	°C	kg/m3	W/(m·K)	kJ/(kg·K)
POK	26	–	–	2300	1.55	1.05
LWK	6	3	6			
WZA	10	12	10			

Table 5. Hydration model parameters

Site	E_a	β	τ	α_u	$Q_{\text{ult}} = Q_{\text{tot}} \cdot \alpha_u$
	J/mol	–	h	–	kJ/kg
POK	61014	0.335	65	0.895	432
LWK	47698	0.372	55	0.971	387
WZA	50107	0.365	56	0.950	391

3.3. Calculation results and comparison to measurements

Obtained results are presented in Figs. 7– 11 below. For test sites that have had two instrumented panels, the results are presented separately, but with time scale origin consistent with measurements commencement.

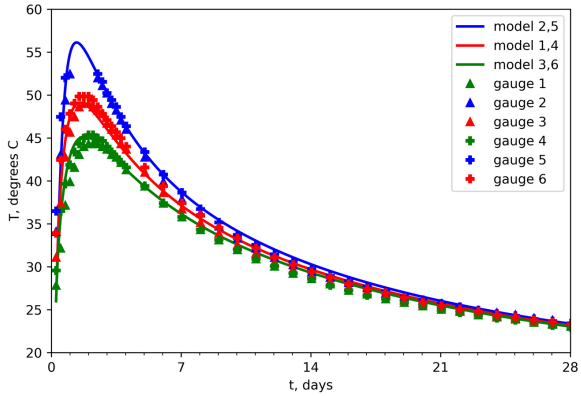

Fig. 7. Comparison of model and measurement results – POK site

Since the parameters of soils are not known, curve fitting was done to find values that are reflected in measurements. It is worth noting that soil parameters influence the tail of the temperature graph i.e., how the concrete temperature approaches equilibrium. At the beginning of concrete curing, the result is dominated by hydration heat discharge. Temperature, especially in the middle of the section, approximates adiabatic conditions.

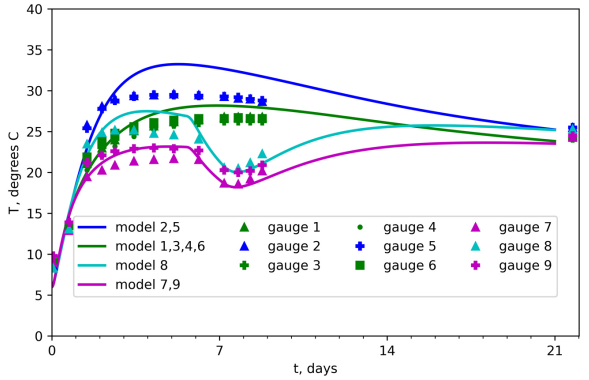

Fig. 8. Comparison of model and measurement results – LWK site – primary panel

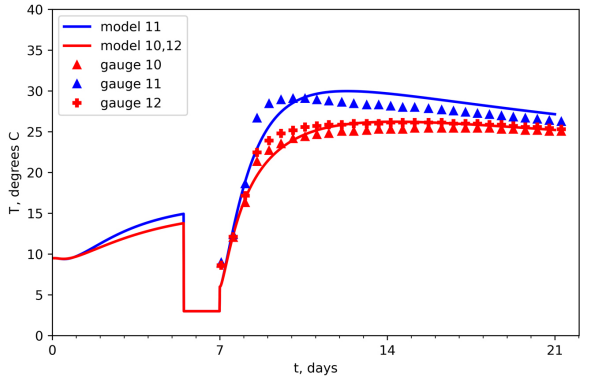

Fig. 9. Comparison of model and measurement results – LWK site – secondary panel

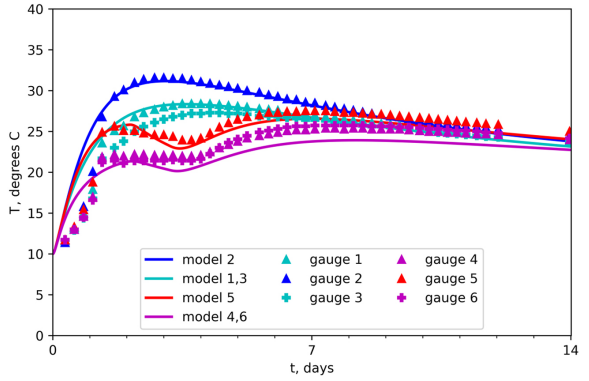

Fig. 10. Comparison of model and measurement results – WZA site – primary panel

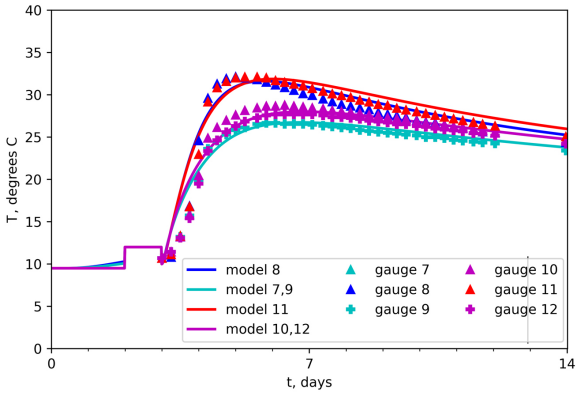

Fig. 11. Comparison of model and measurement results – WZA site – secondary panel

Points on graphs represent measured data. For readability, every 24, 12, and 6 datapoint is plotted for POK, LWK, and WZA respectively. Continuous lines represent model prediction for respective gauges. Each line is marked as "model X" signifying it is referring to gauge X.

For POK test site there is observed non-negligible temperature difference between external gauges on both levels. It has been interpreted as cage installation misalignment resulting in different depths from concrete edge. Model results predict misalignment of 2,5 cm.

There are missing data patches in a few cases. For POK (Fig. 7) this was due to exceeding the measurement range of $1k\Omega$, i.e., the temperature rose above 53°C. For LWK (Fig. 8), a battery malfunction happened twice for one of the dataloggers including once over the holiday period. Only the last measurement was retrieved successfully. Finally, there was an apparent problem with gauges 5–12 at the WZA site (Fig. 10, Fig. 11). The temperature values for fresh concrete indicated 3°C and the temperature graph tail was parallel but lower compared to gauges 1–4. The discrepancy was interpreted as additional resistance measured, probably due to dirty connections. The values were corrected by a resistance value necessary to bring starting temperature to 10°C that agrees with independent measurements on site. While this data should be treated carefully it seems to accord with unmodified values from gauges 1–4 both in terms of graph tail and maximum temperatures reached.

4. Summary and conclusions

The calculation results are in good accord with the measurement data. In most cases the difference between calculated and measured peak temperature values is within ±3°C. For the primary panel on the LWK test site, the differences were higher and reached 5°C.

The method of modeling heat of hydration generation is proven to give a reasonable approximation of real-life situations. A possible improvement is to adopt the method proposed in [20] that takes into account admixtures to concrete like water reducers or retarders.

Based on measurement results from POK and LWK sites embedment depth does not. influence the measured values below 3 m, confirming that heat dissipation in this range is, as expected, 2D heat diffusion problem. For finding the limit of validity of 2D approach for

lower values of embedment more research is necessary. Notably, the difference between gauges in the same level but on the opposite sides of the cage display higher differences than gauges on different levels but on the same side. As model predictions for side gauges are sensitive to distance to concrete face, this observed discrepancy is be attributed to uneven alignment of the cage in the trench on the construction site.

The model considers not only the effects of the single-panel cement hydration but also the sequential execution of the adjacent secondary panel. The idealized assumption that the excavation and concreting happen instantly gives results that accord with the measurements. Based on the analysis of the data it is correct to assume convective heat exchange at constant temperature during slurry trench excavation.

The temperature fall-off is a good indicator to derive thermal soil parameters. In the case of all 3 test sites, the obtained values were the same. When compared to literature, e.g. [23], these values are within given ranges. In deep foundations practice encountered soils are mostly saturated, which narrows down the possible variations of the parameters. It is probable that heat dissipation in concrete is not very sensitive to small-range variations. More attention should be paid to the thermal conductivity of the soil compared to specific heat.

The results of the proposed model cover the whole 2D domain, which can be used in further calculations and considerations toward understanding the stress state in a diaphragm wall at an early age.

4.1. Further research

The approach presented in this article is the baseline to further study the early-age behavior of deep foundations. The next steps include expanding the analysis to the domain of stresses and strains in order to identify possible mechanisms that cause characteristic patterns of cracking like the one presented at the beginning of this article.

References

[1] P.B. Bamforth, *CIRIA Report C766: Control of cracking caused by restrained deformation in concrete*. CIRIA, 2018.

[2] H.L. Le Chatelier, "Sur les changements de volume qui accompagnent le durcissement des ciments (On the changes in volume which accompany the hardening of cements)", *Bulletins de la Société de l'Encouragement pour l'Industrie Nationale*, vol. 5, no. 5, pp. 54–57, 1900.

[3] S. Zhutovsky and K. Kovler, "Effect of water to cement ratio and degree of hydration on chemical shrinkage of cement pastes", in *2nd RILEM International Workshop on Concrete Durability and Service Life Planning*. RILEM, 2009, pp. 47–57.

[4] M. Safiuddin, A.B.M.A. Kaish, C.O. Woon, and S.N. Raman, "Early-age cracking in concrete: Causes, consequences, remedial measures, and recommendations", *Applied Sciences (Switzerland)*, vol. 8, no. 10, 2018, doi: 10.3390/app8101730.

[5] L. Grabowski and M. Mitew-Czajewska, "Early-age thermal-shrinkage cracking in deep foundations", *Studia Geotechnica et Mechanica*, vol. 43, no. S1, pp. 510–520, 2021, doi: 10.2478/sgem-2021-0033.

[6] PN-EN 1992-1-1:2008 Eurokod 2 – Projektowanie konstrukcji z betonu – Część 1-1: Reguły ogólne i reguły dla budynków. PKN, 2008.

[7] D.D. Liou, "Thermal cracking in the diaphragm-wall concrete of Kawasaki Island", in *Thermal Cracking in Concrete at Early Ages*, 1st ed., R. Springenschmid, Ed. CRC Press, 1994, pp. 393–400.

[8] D.D. Liou, "Thermal Effects in large-sized diaphragm wall", *Journal of Performance of Constructed Facilities*, vol. 13, no. 1, 1999, doi: 10.1061/(asce)0887-3828(1999)13:1(17).

[9] M. Wojciechowski, "Shape identification of the jet-grouted column based on the thermal analysis and differential evolution", *Archives of Civil Engineering*, vol. 69, no. 4, pp. 507–518, 2023, doi: 10.24425/ace.2023.147673.

[10] LCPC, *Recommandations pour la prévention des désordres dus ŕ la réaction sulfatique interne – Guide technique (Recommendations for the prevention of disorders due to internal sulfate reaction – Technical guide)*. Paris, 2007.

[11] J. Dunnicliff, *Geotechnical instrumentation for monitoring field performance*. John Wiley & Sons, 1993.

[12] J. Ruiz, A. Schindler, R. Rasmussen, and T. Johnson, "Prediction of heat transport in concrete made with blast furnace slag aggregate", presented at 9th Conference on Advances in Cement and Concrete, Colorado, USA, 2003.

[13] A.K. Schindler, "Effect of temperature on hydration of cementitious materials", *ACI Materials Journal*, vol. 101, no. 1, pp. 72–81, 2004, doi: 10.14359/12990.

[14] P. Freiesleben Hansen and E.J. Pedersen, "Maleinstrument til kontrol af betons haerdning (Measuring instrumentation for checking concrete's hardening)", *Nord Betong*, no. 1, pp. 21–23, 1977.

[15] J. Poole, "Modeling temperature sensitivity and heat evolution of concrete", University of Texas at Austin, 2007.

[16] FIB, *Draft CEB guide to durable concrete structures*. FIB – International Federation for Structural Concrete, 1985.

[17] G. De Schutter and L. Taerwe, "Degree of hydration-based description of mechanical properties of early age concrete", *Materials and Structures/Materiaux et Constructions*, vol. 29, no. 190, pp. 335–344, 1996, doi: 10.1007/bf02486341.

[18] A.K. Schindler and K.J. Folliard, "Heat of hydration models for cementitious materials", *ACI Materials Journal*, vol. 102, no. 1, pp. 24–33, 2005, doi: 10.14359/14246.

[19] R.H. Mills, "Factors influencing cessation of hydration in water cured cement pastes", *Highway Research Board Special Report*, no. 90, pp. 406–424, 1966.

[20] K.A. Riding, J.L. Poole, K.J. Folliard, M.C.G. Juenger, and A.K. Schindler, "Modeling hydration of cementitious systems", *ACI Materials Journal*, vol. 109, no. 2, pp. 225–234, 2012, doi: 10.14359/51683709.

[21] J. Crank, *The mathematics of diffusion*. Clarendon Press, 1975.

[22] G.D. Smith, *Numerical solution of partial differential equations: finite difference methods*. Oxford Applied Mathematics and Computing Science Series. Clarendon Press, 1985.

[23] T.R. Oke, *Boundary layer climates*, 2nd ed. Routledge, 2002.

Dyssypacja ciepła hydratacji w ścianach szczelinowych

Słowa kluczowe: głębokie fundamentowanie, ściany szczelinowe, ciepło hydratacji, wczesne zarysowanie termiczno-skurczowe, beton kontraktorowy

Streszczenie:

Artykuł koncentruje się na badaniu złożonych procesów dyssypacji ciepła w ścianach szczelinowych podczas hydratacji betonu, co jest istotne w inżynierii budowlanej. Przeprowadzono eksperymenty na trzech różnych placach budowy w Polsce, gdzie ściany szczelinowe miały różne grubości od 1 do 1,5 metra. Zebrane pomiary porównano z modelem numerycznym, który wykorzystuje metodę różnic skończonych obejmował również zmienność parametrów w czasie na skutek wykonania sąsiedniej sekcji ściany szczelinowej. Model wykazał znaczną zgodność z rzeczywistymi temperaturami, co potwierdza jego trafność predykcyjną. Chociaż zaobserwowano pewne różnice, głównie w granicach

±3°C, metoda skutecznie oddaje realne warunki. Zalecenia dotyczące ulepszeń modelu obejmują uwzględnienie domieszek do betonu oraz optymalizację modelowania sekwencji wykonania paneli sąsiednich. Istotnym wnioskiem są również informacje o parametrach termicznych gruntu i ich wpływie na dyssypację ciepła w betonie. Badania te stanowią podstawę dla dalszych badań nad zachowaniem konstrukcji w początkowych fazach wiązania betonu fundamentów głębokich. Celem jest rozszerzenie analizy na pole naprężeń i odkształceń, co pozwoli zrozumieć charakterystyczne zarysowania obserwowane w ścianach szczelinowych.

Received: 2023-12-21, Revised: 2024-02-25